



Energy-dispersive Laue diffraction by means of a pnCCD detector coupled to a CsI(Tl) scintillator using ultra-hard X-ray synchrotron radiation

Mohammad Shokr,^{a,*} Amir Tosson,^a Ali Abboud,^a Alaa Algashi,^a Dieter Schlosser,^b Robert Hartmann,^b Manuela Klaus,^c Christoph Genzel,^c Lothar Strüder^{a,b} and Ullrich Pietsch^a

Received 19 October 2018

Accepted 3 May 2019

Edited by A. F. Craievich, University of São Paulo, Brazil

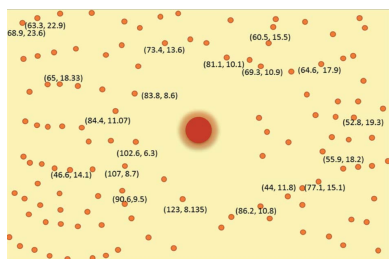
Keywords: PnCCD detector; CsI(Tl) scintillator; X-ray Laue diffraction; energy-dispersive X-ray detectors; ultra-hard X-ray synchrotron radiation.

^aUniversität Siegen, Walter-Flex Strasse 3, 57062 Siegen, Germany, ^bPNSensor GmbH, Otto-Hahn-Ring 6, D-81739 München, Germany, and ^cHelmholtz-Zentrum Berlin für Materialien und Energie, Albert-Einstein Strasse 15, 12489 Berlin, Germany. *Correspondence e-mail: shokr@physik.uni-siegen.de

The lattice parameters and unit-cell orientation of an SrLaAlO₄ crystal have been determined by means of energy-dispersive X-ray Laue diffraction (EDLD) using a pnCCD detector coupled to a columnar structure CsI(Tl) scintillator in the energy range between 40 and 130 keV. By exploiting the high quantum efficiency (QE) achieved by this combined detection system for hard X-rays, a large number of Bragg reflections could be recorded by the relatively small detector area, allowing accurate and fast determination of the lattice parameters and the moduli of the structure factors. The experiment was performed on the energy-dispersive diffraction (EDDI) beamline at the BESSY II synchrotron using a pnCCD detector with 128 × 128 pixels. Since the energies and positions of the Laue peaks can be recorded simultaneously by the pnCCD system, the tetragonal structure of the investigated specimen was determined without any prior information. The unit-cell parameters and the angles between the lattice vectors were evaluated with an accuracy of better than 0.7%, while the structure-factor moduli of the reflections were determined with a mean deviation of 2.5% relative to the theoretical values.

1. Introduction

The pnCCD detector has been used recently for the investigation of single crystals and polycrystalline materials at X-ray energies below 30 keV (Send *et al.*, 2012; Leitenberger *et al.*, 2008; Kirkwood *et al.*, 2017). However, the low quantum efficiency (QE) of silicon at high energies limits the use of silicon-based charge-coupled devices for applications that require ultra-hard X-rays. In order to avoid this limitation, a columnar structured CsI(Tl) scintillator has been coupled to the pnCCD detector, improving the QE of the system to around 50% at 100 keV instead of 1% for the naked pnCCD (Schlosser *et al.*, 2016). This so-called columnar CsI scintillator has the capability of channelling scintillation light towards the exit surface through total internal reflection, reducing the divergence of visible photons emitted from the scintillator back to the silicon photon detector. In addition, this structure helps to reduce the depth of interaction-dependent blurring and results in a narrow spatial resolution. The system used in our experiment was developed by PNSensor GmbH in Munich and consists of a micro-columnar thallium-doped caesium iodide [CsI(Tl)] scintillator with a volume of 12 mm × 12 mm × 0.7 mm and a density of 4.5 g cm⁻¹, attached to the back of a 0.45 mm-thick pnCCD with 128 × 128 pixels and a



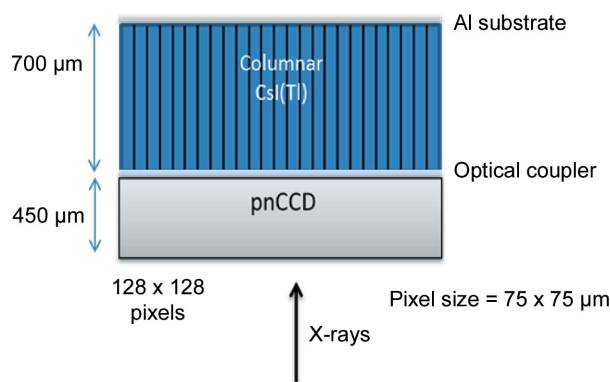


Figure 1

The structure of the detection system. In this configuration the detector is front illuminated (pixels side) and the low-energy photons below 15 keV are almost totally absorbed by the CCD. X-rays with higher energies are stopped by the scintillator with a high QE.

pixel size of $75\ \mu\text{m} \times 75\ \mu\text{m}$. The CsI(Tl) is coupled to the pnCCD with a $50\ \mu\text{m}$ thin silicone protection pad covered with optical grease (Fig. 1). The detector configuration is described in detail by Schlosser *et al.* (2017).

Using the front-illuminated geometry (pixelated side), low-energy photons (below 10 keV) are absorbed nearly completely by the pnCCD as the QE of Si in this energy range is close to 100%. This type of detection is so-called ‘direct detection’. As the energy of the incident photons increases above 10 keV, the QE of the silicon in the pnCCD decreases and hence more photons can traverse the Si chip and reach the CsI(Tl) scintillator at the back. The stopping power of the scintillator material is close to 100% at energies of up to 40 keV, 90% at 60 keV and 50% at 100 keV (Jing *et al.*, 1998; Nagarkar *et al.*, 1998). The interaction between the X-ray photons and the scintillator results in the generation of optical photons where 90% of them are back-reflected and absorbed by the pnCCD. This detection process is called ‘indirect detection’ of X-rays. The excellent spectroscopic performance of the coupled system and the good spatial resolution of the pnCCDs in combination with the scintillator were measured with a frame rate of up to 400 frames per second, demonstrating their long time stability and radiation hardness. In previous work we have shown that the energy resolution of directly detected Laue peaks with energies ranging between 40 and 90 keV is of the order of 0.7–0.9%, while the energy resolution of the indirect detection of these peaks is between 16.5 and 18.5% (Shokr *et al.*, 2017). It has also been shown that the error in determining the scattering intensity from the indirect detection of these peaks is less than 1.5%. This achievement makes the combined system favourable for the determination of lattice parameters and use in the hard X-ray range.

Using energy-insensitive area detectors and pink X-ray beams, the determination of crystal lattice parameters in macromolecular crystallography (Helliwell, 1984; Cornaby *et al.*, 2010) and Laue micro-diffraction of inorganic samples (Dejoie *et al.*, 2013; Hofmann *et al.*, 2012) is possible only considering prior knowledge of the material. On the other hand, energy-dispersive point detectors (EDDs) enable measurement of a complete energy spectrum but detection of

different Laue spot positions requires detector movement along the plane of detection in order to detect the spots sequentially. This strategy is generally time consuming. Other detectors like the PILATUS or XPAD detectors do not perform a precise measurement of the X-ray signal amplitude, but they count the number of measured signal amplitudes above a given discriminator threshold (Kraft *et al.*, 2009; Medjoubi *et al.*, 2012). In a white X-ray spectrum or in a spectrum with several X-ray lines they cannot be used as a reliable simultaneous energy-dependent X-ray counter. Simultaneous indexing of several Laue reflections is impossible. In contrast, pnCCDs allow for the efficient combination of two-dimensional position and energy resolution of incident X-rays.

So far, the pnCCD has been used for the determination of crystal parameters and structure-factor moduli in the energy range 5–35 keV, except in the work by Send *et al.* (2016) where these parameters were determined for GaAs using a pnCCD without a scintillator in the hard X-ray regime up to 140 keV. In addition to well detected low-energy spots, the high-energy Laue spots could be detected with very low counting statistics. In the end the structure-factor magnitudes of the high-energy reflections were calculated with an average deviation of more than 11% compared with the theoretical values. However, it was shown by Shokr *et al.* (2017) that this accuracy can be improved to less than 1.5% when the determination of the structure-factor modulus is based mainly on the indirect detection of peaks by the pnCCD + CsI(Tl) system.

The use of hard X-rays for Laue diffraction experiments profits from the fact that the part of the Ewald sphere that is cut by the detection plane is rather flat, accessing a large reciprocal-space volume simultaneously (Liss *et al.*, 2003; Wu *et al.*, 2016). In this way, the density of Laue spots to be collected by the relatively small pnCCD detector area is significantly enhanced compared with previous experiments. Furthermore, the lower photoelectric interaction in the hard X-ray regime leads to less radiation damage in crystalline materials (Jakoncic *et al.*, 2006).

The solid-state physics group at the University of Siegen is equipped with a frame-store modular pnCCD combined with a CsI(Tl) scintillator with the dimensions mentioned above, and the camera is used for hard X-ray applications such as crystal structure determination, single-grain analysis of polycrystalline samples and texture analysis. In this work we show the determination of the unit-cell parameters and orientation of a tetragonal SrLaAlO₄ crystal without any prior information by means of an energy-dispersive Laue diffraction experiment (EDLD) using the pnCCD + CsI(Tl) system and a white X-ray beam with an energy ranging between 40 and 130 keV. It will be demonstrated that the spatial resolution and spectroscopic performance of the indirect detection of this hybrid detector in this energy range is sufficient for the precise determination of unit-cell parameters and lattice-vector orientation. For fast data analysis, a GPU-based algorithm was applied which executes all recorded reflections in parallel and in real time (Alghabi *et al.*, 2014). With the aim of saving time on the scanning process when required and improving the

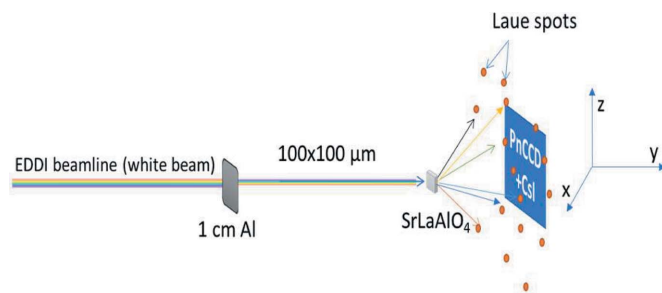


Figure 2
The setup of the Laue diffraction experiment on the EDDI beamline. The sample was illuminated by a white X-ray beam with a size of $100 \times 100 \mu\text{m}$ attenuated by means of 1 cm of Al, and the plane in front of the sample was scanned by the detector to detect the Laue spots that lie on this plane.

spatial resolution, it is worth mentioning that the development of this detector system for a larger area (three times that of the system used here) and a smaller pixel size ($48 \times 48 \mu\text{m}$) is in progress.

2. Experiment and data extraction

2.1. Experiment setup and detector settings

Fig. 2 shows the setup of the Laue diffraction experiment on the EDDI beamline of the BESSY II storage ring in Berlin. In order to avoid radiation damage of the detector and to operate the detector in the so-called single counting mode (Send *et al.*, 2013), the primary white X-ray beam with an energy range of 1–130 keV generated by a 7 T multipole wiggler (Genzel *et al.*, 2007) was attenuated by means of a 1 cm-thick aluminium plate. The presence of the Al absorber in front of the sample cuts off photons with energies below 40 keV. The sample crystal with [001] orientation was illuminated by a $100 \mu\text{m} \times 100 \mu\text{m}$ beam. In order to simulate a larger detector window virtually, an area of $5 \text{ cm} \times 3 \text{ cm}$ of the xz plane at a distance of 6 cm in front of the sample was scanned by the detector. The average count rate was about 33 000 events per second per entire area such that the detector was operated at a frame rate of 400 Hz. The event detection threshold was set to 4σ where $\sigma = 5.5 e^-$ (r.m.s.) is the equivalent noise charge in the selected gain mode of the detector including thermal and electronic noise components.

2.2. Data collection

A scheme of the collected Laue pattern is shown in Fig. 3 in which about 130 spots have been recorded. Generally, Laue spots with energies less than about 90 keV were detected directly by the p-nCCD. At the same time, these spots are also detected indirectly as the photons which did not interact with the p-nCCD traverse the silicon chip and interact with the scintillator material with a high QE and generate low-energy photons. These optical photons (λ about 550 nm) are collected again by the p-nCCD with a high QE. In contrast, spots with energies higher than 90 keV cannot be detected directly by the p-nCCD due to the low QE but they are detected indirectly after interaction with the scintillator.

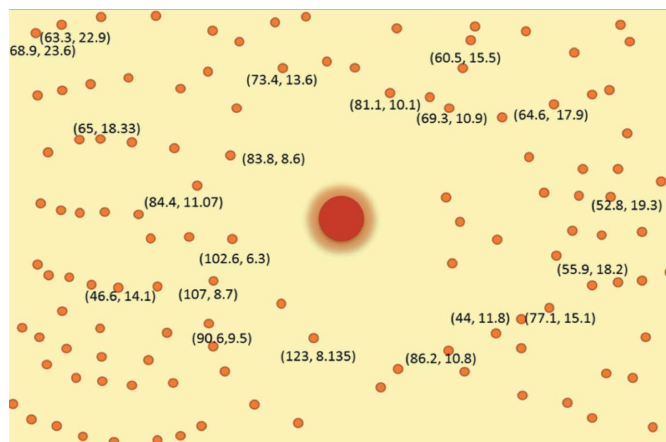


Figure 3
The Laue pattern generated by the SrLaAlO_4 crystal recorded by the p-nCCD + CsI(Tl). Some of the Bragg reflections were detected directly and indirectly at the same time, while others with higher energies were just detected indirectly. The energy and Bragg angle ($E, 2\theta$) are shown beside some spots.

Once a photon interacts directly with the p-nCCD and is converted to an electron cloud, it can be collected by one pixel (single-pixel events) or distributed over neighbouring pixels (double-, triple- or quadruple-pixel events), depending on the cloud size (proportional to the photon energy) and conversion position (Abboud *et al.*, 2013). However, when the photon is detected indirectly, the generated electron cloud is the result of the sum of many scintillation photons which typically spread over more than ten pixels. The different event size can be used later to distinguish between direct and indirect events.

A further advantage of indirect detection is the improved position resolution of the Laue spots. The high statistics of the indirect events give rise to intense spots with well defined peak centres. Fig. 4 shows intensity images of some Laue spots recorded at one of the scan positions during the experiment: in Fig. 4(a) all events are taken into account (direct and indirect events), while in Fig. 4(b) only events with a size less than five pixels (direct events) are taken into account. This clearly

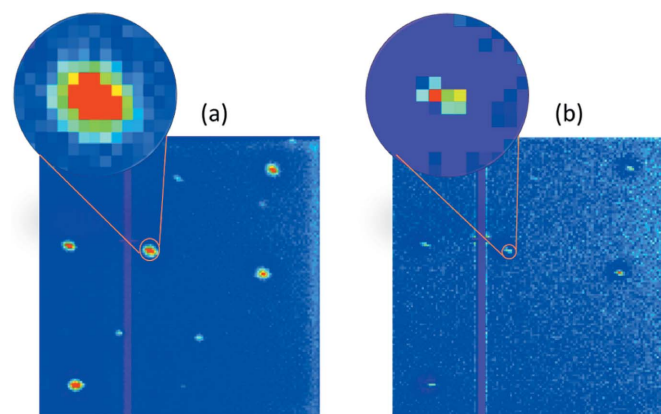


Figure 4
Laue patterns of a detector area (128×128 pixels). (a) All direct and indirect events. (b) Only events from direct detections. The vertical lines through the images are due to three defect channels in the detector.

demonstrates the higher efficiency of peak location and peak intensity obtained by considering the indirect events.

2.3. Spectral analysis

When X-rays impinge on the pnCCD they convert their total energy to free charge carriers and heat. Although the band-gap energy of silicon is $E = 1.12$ eV, the mean energy needed to generate an electron–hole pair is 3.67 eV (Devanathan *et al.*, 2006) The number of generated electrons is proportional to the interacting X-ray photon and they are then directly guided to a low-capacitance readout node. At the scintillator level, X-rays hitting the CsI material excite equally electrons from the valence to the conduction band or to the activator states of the dopants, here Tl. They recombine through the activator levels in the forbidden band gap, emitting a photon with a wavelength of 550 nm. These photons are isotropically radiated from their position of generation but a significant number of them are back reflected towards the silicon photo-detector. Those photons that do not reach the photo-detector directly and do not match the total reflection conditions of the scintillator–pnCCD system are lost. The QE

for optical photons in the radiation entrance window of the pnCCD, including absorption in the separating silicone pad and the optical grease, is approximately 85% for photons coming from the scintillator. Comparing the two detection processes of the pnCCD and CsI(Tl), direct conversion in silicon leads to an output signal about six times higher than the indirect signal from the CsI.

The spectrum integrated over all events is shown in Fig. 5 in analogue-to-digital units (ADU). It contains the direct detection of the $K\alpha$ and $K\beta$ emission lines of Sr and La (elements of the illuminated crystal) located at 1793, 2010, 4252, 4830 and 4950 ADU, corresponding to 14.1, 15.8, 33.2, 37.8 and 38.7 keV, respectively. The spectrum also includes the $K\alpha$ and $K\beta$ lines of I and Cs (elements of the scintillator) located at 3647, 4125, 3950 and 4472 ADU, corresponding to 28.4, 30.7, 32.2 and 34.9 keV, respectively. These direct peaks were resolved with an energy resolution of between 0.75 and 0.9% at the selected gain of the detector and they were used to calibrate the channel numbers (from ADU to electronvolts), while the peak between 250 and 750 ADU is the result of the convolution of their indirect peaks. In order to identify the Bragg energies, the spectra of all detected spots were extracted from an area of 5×5 pixels around the centre of each spot (Abboud *et al.*, 2013; Granato *et al.*, 2013). If the Laue spot is detected directly and indirectly at the same time, the respective spectrum will contain two Bragg peaks, one at an energy corresponding to direct detection of the spot, and another peak at lower energy (typically between 1 and 35 keV) corresponding to indirect detection. After calibration the peak positions can be converted to the corresponding incoming photon energy.

Fig. 6 shows two examples of recorded spectra for two different types of spot: Fig. 6(a) is the spectrum of a spot detected directly and indirectly at the same time, while Fig. 6(b) is the spectrum of another spot just detected indirectly. Events with a size between 1×1 and 10×10 pixels (non-recombined events) measure direct and indirect events, respectively. The Bragg peak from direct detection in Fig. 6(a)

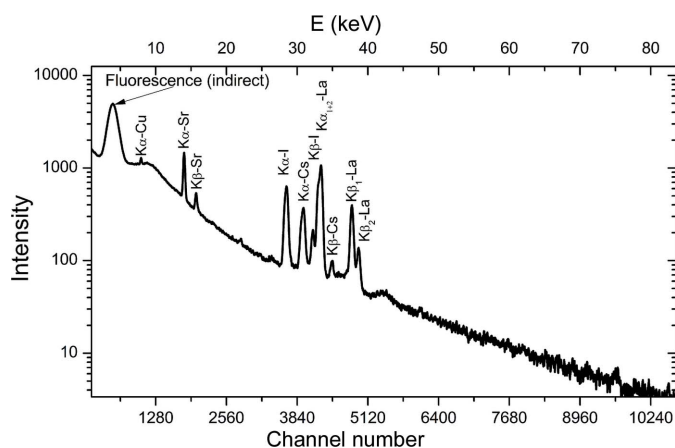


Figure 5 The spectrum of all direct and indirect events.

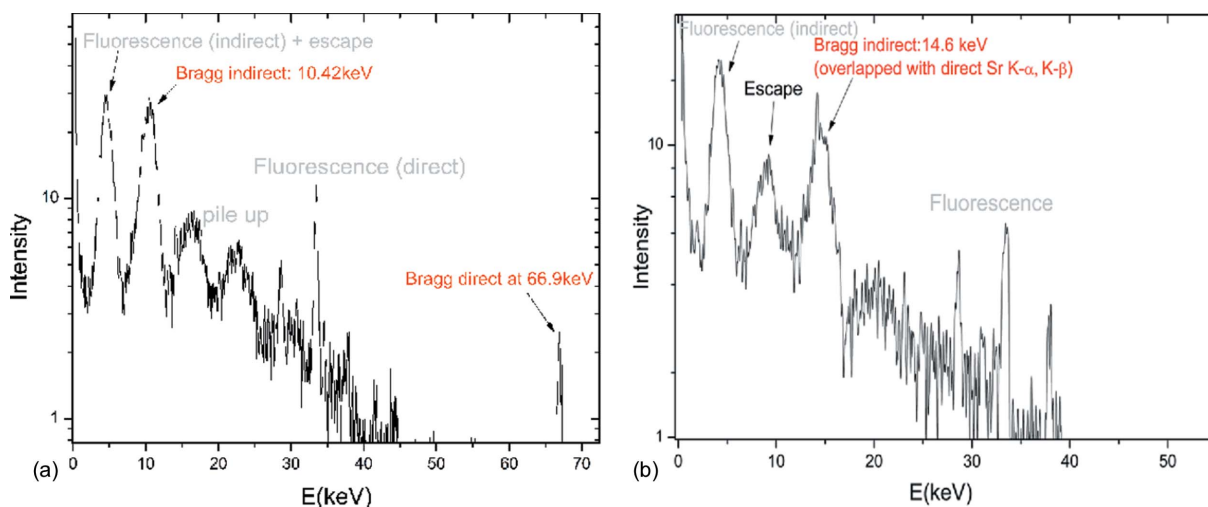


Figure 6 Spectra of two Laue spots given by pnCCD. (a) Data detected directly and indirectly at the same time. (b) Data just detected indirectly.

is located at an energy of 66.9 keV with a FWHM of 539 eV, while the peak referring to indirect detection is located at 10.42 keV with a FWHM of 2.07 keV represented on the energy scale of the direct events. Fig. 6(b) is an example spectrum of the indirectly detected spots. This spectrum does not contain the direct peak due to its high energy, while its indirect peak appears at an energy of 14.6 keV. This peak overlaps with the $K\alpha$ and $K\beta$ lines of Sr at 14.1 and 15.8 keV, respectively. The spectrum also contains an indirect fluorescence peak at 4.2 keV followed by an escape peak from the indirect Bragg peak at 8.99 keV. The direct peaks of the fluorescence lines between 27 and 37 keV are also visible in this spectrum. The energy of the indirect Bragg peak is proportional to the energy of the incident photon, and hence one needs to find the relation between the incident photon energy (direct energy) and the indirect energy which usually depends on the selected gain of the detector. The energies of all spots that are detected directly and indirectly at the same time, like the case of Fig. 6(a), are used to find the functional relation. The direct energies of all indirectly detected spots can then be identified and the intensities of these spots can be calculated from the indirect peaks, taking into account the QE of CsI(Tl) at the incident energy and the escape and pile up peaks. As an example, the direct photon energy of the spectrum shown in Fig. 6(b) was determined to be 92.5 keV. It is noteworthy that no Compton events are involved in the indirect spectra since Compton electrons cannot spread over more than one pixel, whereas only events with a size larger than ten pixels are included in these spectra.

3. Determination of lattice parameters and unit-cell orientation

3.1. Calculation of lattice parameters

As soon as the spot energies are identified, a scattering vector \mathbf{q} for each Bragg reflection can be assigned by the difference between the outgoing (subscript f) and incoming (subscript i) wavevectors

$$\mathbf{q} = \mathbf{k}_f - \mathbf{k}_i, \quad (1)$$

such that

$$|\mathbf{k}_f| = |\mathbf{k}_i| = \frac{2\pi}{\lambda} = \frac{E}{\hbar c}, \quad (2)$$

where λ is the wavelength of the spot, E its energy, \hbar is the Planck constant divided by 2π and c is the speed of light. Every Laue spot collected by the detector is characterized by its intensity, I , energy, E , and spatial coordinates at the detector plane, here (x, z) .

$$\hbar c \mathbf{q} = \hbar c \begin{pmatrix} q_x \\ q_y \\ q_z \end{pmatrix} = \frac{E}{s} \begin{pmatrix} x \\ y - s \\ z \end{pmatrix}, \quad (3)$$

where z is the sample-to-detector distance and s is the distance between the sample and the Laue spot on the detector plane:

$$s = (x^2 + y^2 + z^2)^{1/2}. \quad (4)$$

In our experiment the measured part of the reciprocal lattice of the crystal is confined in a cuboid with ranges $-13 \leq q_x \leq 13 \text{ \AA}^{-1}$, $-4 \leq q_y \leq 0 \text{ \AA}^{-1}$ and $-8 \leq q_z \leq 8 \text{ \AA}^{-1}$. The error $\sigma \mathbf{q}$ depends on the precision in the position and energy of the spot such that

$$\delta q_x = \frac{|x|}{s} \frac{\delta E}{\hbar c} + \frac{E}{s^3 \hbar c} [(y^2 + z^2) \delta x + |xy| \delta y + |xz| \delta z], \quad (5)$$

$$\delta q_y = \frac{(s - y) \delta E}{s \hbar c} + \frac{E}{s^3 \hbar c} [(x^2 + z^2) \delta y + |yx| \delta x + |yz| \delta z], \quad (6)$$

$$\delta q_z = \frac{|z|}{s} \frac{\delta E}{\hbar c} + \frac{E}{s^3 \hbar c} [(x^2 + y^2) \delta z + |zx| \delta x + |zy| \delta y]. \quad (7)$$

The energy of the reflections was resolved with a standard deviation ranging between 0.6 and 0.8% considering the Gaussian fit to the measured Bragg peak energy. The high intensities of the reflections due to indirect detection improve the spatial uncertainty to less than one pixel. Consequently, using equations (5), (6) and (7), the components of the scattering vector \mathbf{q} associated with the reflections could be resolved with absolute accuracies of $\delta q_x < 0.15 \text{ \AA}^{-1}$, $\delta q_y < 0.08 \text{ \AA}^{-1}$ and $\delta q_z < -0.15 \text{ \AA}^{-1}$.

The scattering vector corresponding to the evaluated peak centres in terms of position and energy is equal to a reciprocal-lattice vector of the sample:

$$\mathbf{q} = \mathbf{G} = h\mathbf{b}_1 + k\mathbf{b}_2 + l\mathbf{b}_3, \quad (8)$$

where h , k and l are the Miller indices of the reflection that need to be determined and \mathbf{b}_i are the reciprocal basis vectors in the externally defined coordinate system. In order to find the lattice constants of SrLaAlO₄, we applied the method used by Send *et al.* (2009) in which the Minkowski-reduced basis (Minkowski, 1891) of the measured reciprocal lattice was computed by crystallographic reduction (Delaunay, 1933; Gauss *et al.*, 1986) and least-squares refinement of sets of three non-collinear scattering vectors (\mathbf{q}_1 , \mathbf{q}_2 , \mathbf{q}_3) providing a complete indexing of all recorded reflections. Because of the large number of events included in each reflection which requires a relatively long execution time, a new GPU-based algorithm was developed and used for the computing of this method (Tosson *et al.*, 2019). Depending on the parallel computation technique, a speed-up factor of up to 4 was obtained compared with the serial algorithm. This algorithm has the single-instruction multiple-threads (SIMT) style (Lindholm *et al.*, 2008) and consists of two stages. (i) Parameter calculations, in which the essential parameters (*e.g.* energy, diffraction angle, d spacing, possible Miller indices list *etc.*) for each localized reflection are calculated. Each thread processes a single reflection, saving the final output in a data container for further calculations. (ii) The main core, in which the main method is applied. The localized reflections are divided into threefold subsets covering all possible mutations. Using the output generated by the previous stage, each subset is processed by a single thread. The reciprocal basis vectors are then obtained,

$$\mathbf{b}_1, \mathbf{b}_2, \mathbf{b}_3 = \begin{pmatrix} 1.507(5) & 0.339(3) & 0.197(1) \\ 0.164(1) & 1.286(4) & -0.312(2) \\ -0.734(3) & 1.007(3) & 0.334(2) \end{pmatrix} \text{\AA}^{-1}, \quad (9)$$

and hence the basis vectors in the real crystallographic axes can be calculated,

$$\mathbf{a}_1, \mathbf{a}_2, \mathbf{a}_3 = \begin{pmatrix} 3.341(12) & 0.781(5) & 4.981(15) \\ 0.382(4) & 2.913(11) & -7.932(20) \\ -1.612(7) & 2.255(8) & 8.450(23) \end{pmatrix} \text{\AA}. \quad (10)$$

The unit cell obtained is shown in Fig. 7. Subsequently, the lattice constants and enclosed angles of the crystal are defined:

$$|\mathbf{a}_1| = 3.7331(7) \text{\AA}, \quad (11)$$

$$|\mathbf{a}_2| = 3.762(8) \text{\AA}, \quad (12)$$

$$|\mathbf{a}_3| = 12.613(18) \text{\AA}, \quad (13)$$

$$\alpha = 89.64(24)^\circ, \quad (14)$$

$$\beta = 90.21(36)^\circ, \quad (15)$$

$$\gamma = 89.89(25)^\circ. \quad (16)$$

The evaluated data are in good agreement with the literature values for the tetragonal structure of SrLaAlO₄, with standard deviations of 0.1, 0.2 and 0.7% for the lattice constants and 0.02, 0.23 and 0.4% for the enclosed angles, respectively. This accuracy is better than that obtained previously by Send *et al.* (2009), even though white synchrotron radiation with an energy of less than 35 keV has been used. This improvement can be correlated with the higher number of Laue spots detected within a wide energy range and the improved count rate of these spots due to the improvement in the detector QE. Once the lattice parameters and scattering vector of each reflection have been determined, the Laue pattern can be indexed entirely using Laue equations:

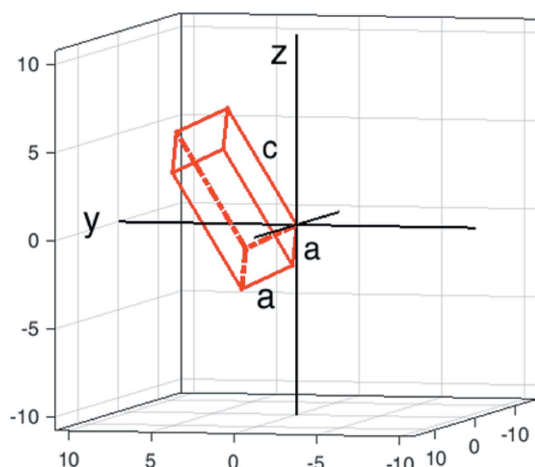


Figure 7
The unit cell of tetragonal SrLaAlO₄ determined experimentally by EDLD using pnCCD + CsI(Tl).

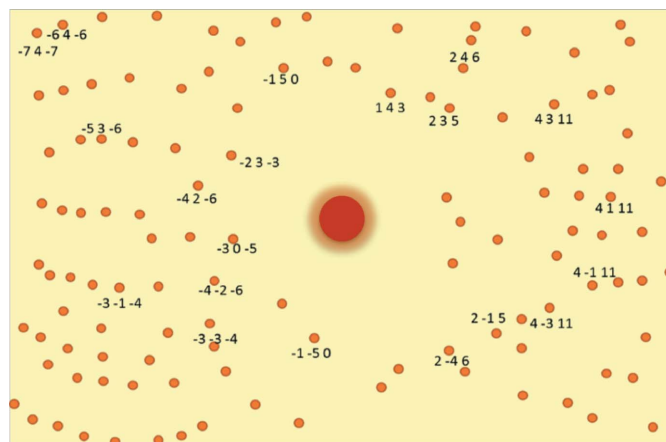


Figure 8
Miller indices of the Laue pattern. All reflections have been indexed using Laue equations.

$$h_i = \frac{\mathbf{q}_i \cdot \mathbf{a}_1}{2\pi}, \quad k_i = \frac{\mathbf{q}_i \cdot \mathbf{a}_2}{2\pi}, \quad l_i = \frac{\mathbf{q}_i \cdot \mathbf{a}_3}{2\pi}. \quad (17)$$

Only a few Miller indices are shown on the Laue pattern in Fig. 8 to keep the figure as clear as possible, while more reflections will be shown in a separate table in the next subsection. The spectra of some spots contain two peaks at energies E and $2E$ corresponding to the first- and second-order reflections, respectively. In this case only the first-order reflection has been taken into account and the Miller indices are calculated based on this energy. However, if E is less than 40 keV (the lower limit of the incident energy), only the second-order reflections ($2E$) can be scattered from the crystal as E has been absorbed by the Al absorber. This leads to second-order Miller indices. For example, spot $-6\ 4\ -6$ has an energy of 63.3 keV at an angle of 22.9° , instead of the $-3\ 2\ -3$ reflection at the same angle with an energy of 31.65 keV, as this energy is not included in the energy range used.

3.2. Moduli of the structure factors

It has been shown by Shokr *et al.* (2017) that the moduli of the structure factors can be calculated experimentally with a relatively high accuracy when the intensities of the reflections are extracted from the indirect peaks rather than the direct peaks. Experimentally, the squared modulus of the structure factor of a reflection hkl is given by

$$|F_{hkl}^{\text{exp}}|^2 = \frac{I_{hkl}}{C I_0 L P A}, \quad (18)$$

where C denotes a scale factor, I_0 is the intensity of the incident white X-ray beam at the diffracted wavelength and $I_{hkl} = I/\varepsilon$ is the intensity of the Bragg peak, with I being the measured integrated intensity of this reflection and ε the QE. L is the Lorentz factor which takes into account that, in real X-ray diffraction experiments, the Bragg condition is not fulfilled by just one specific wavelength λ and one single incident angle θ , but within narrow wavelength and angular bands enclosing these values. In our case of a spatially fixed crystal exposed to white X-rays, L is defined as (Lange, 1995)

$$L = \left(\frac{\lambda}{\sin \theta} \right)^2. \quad (19)$$

P is the polarization factor arising from the polarization effects associated with the nature of the incident beam and can be written as (Send, 2013)

$$P = \frac{1}{2} (1 + \cos^2 2\theta) - \frac{1}{2} \tau \cos 2\rho \sin^2 2\theta. \quad (20)$$

While the first term of equation (20) denotes the contribution of an unpolarized X-ray beam, the second term describes the attenuation of the scattered intensity due to the polarization of the synchrotron radiation. τ is the degree of polarization given by the ratio of the difference between the parallel and perpendicular components of the polarization direction (relative to the plane of the electron orbit in the storage ring) to their summation:

$$\tau = \frac{I_{\parallel} - I_{\perp}}{I_{\parallel} + I_{\perp}}. \quad (21)$$

However, the perpendicular component I_{\perp} almost vanishes for bending-magnet radiation and hence $\tau \simeq 1$. The angle ρ denotes the position of the Laue spot on the detector plane such that

$$\rho = \arctan\left(\frac{z}{x}\right). \quad (22)$$

In our detection range the applied polarization factors have values between 0.9 and 1. The last term in equation (18), A , takes into account the absorption effects along the path of the diffracted beam inside the crystal.

Since all the reflections have been indexed and the atomic coordinates of the crystal are known from the literature (Villars & Cenzual, 2012), the theoretical structure factors F_{hkl}^{theo} could be calculated (Wilson, 1949):

$$\begin{aligned} F_{hkl}^{\text{theo}} &= \sum_j (f_j)_T \exp(-i\mathbf{G}_h \cdot \mathbf{k} \mathbf{r}_j) \\ &= \sum_j (f_j)_T \exp[-2\pi i(hx_j + ky_j + lz_j)], \end{aligned} \quad (23)$$

with x_j , y_j and z_j being the coordinates of atom j within the unit cell, h , k and l the Miller indices of the reflection plane and $(f_j)_T$ the temperature-corrected atomic scattering factor of the form

$$(f_j)_T = f_j \exp\left(\frac{-B_j \sin^2 \theta}{\lambda^2}\right). \quad (24)$$

Here, f_j is the atomic form factor of atom j which can be found in the *International Tables for Crystallography* (Brown *et al.*, 2004). The exponential term represents the Debye–Waller factor including the Bragg angle θ , the wavelength λ of the relevant reflection and the so-called temperature factor

$$B_j = 8\pi^2 \langle u_j^2 \rangle, \quad (25)$$

where $\langle u_j \rangle$ is the mean-square displacement of atom j (Villars & Cenzual, 2012) due to atomic vibrations.

After determining $|F_{hkl}^{\text{theo}}|$, the obtained experimental values $|F_{hkl}^{\text{exp}}|$ are then normalized to the theoretical values where the scale factor C was defined by the least-squares method. It is challenging to calculate $|F_{hkl}|$ experimentally with an error as low as possible. One can see from equation (18) that the error in the structure-factor magnitude of a given hkl reflection depends strongly on the error propagation from the intensity calculation. This includes the systematic (subscript sys) and statistical (subscript stat) errors such that the total error propagation for the primary intensity is

$$\sigma_{I_{hkl}} = \sigma_{\text{sys}} + \sigma_{\text{stat}} = \frac{I}{\varepsilon^2} \sigma_{\varepsilon} + \frac{I^{1/2}}{\varepsilon}, \quad (26)$$

where σ_{ε} is the error in ε which is calculated from the respective attenuation coefficients of Si and CsI(Tl). It is worth mentioning that only the photoelectric contribution of the QE is taken into account here, as the Bragg peaks in the spectrum are generated by photoelectric interaction. Finally, the relative error in the calculated diffracted intensity can be written as

$$\frac{\sigma_{I_{hkl}}}{I_{hkl}} = \frac{(\varepsilon I_{hkl} / \varepsilon^2) \sigma_{\varepsilon} + (\varepsilon I_{hkl})^{1/2} / \varepsilon}{I_{hkl}} = \frac{\sigma_{\varepsilon}}{\varepsilon} + \frac{1}{(I_{hkl} \varepsilon)^{1/2}}, \quad (27)$$

which makes the QE the main factor affecting the precision of the I_{hkl} calculations and subsequently the accuracy of the structure-factor magnitude determination.

Table 1 shows a list of the recorded reflections with their Miller indices, Bragg angles, energies and interplanar distances, and their corresponding experimental and theoretical structure-factor magnitudes. As discussed before, the error σ_F depends on the deviation in the intensity calculation, which itself depends strongly on the QE of the detection material as well as on the intensity of the spot [equation (27)], such that a higher efficiency and higher intensity lead to higher precision. With the aim of having the best possible accuracy in the calculation of the structure-factor magnitudes, the diffracted intensities I_{hkl} were extracted from the indirect peaks where the detected intensities, I , were much higher than those found in the direct peaks, in addition to the high QE of the CsI(Tl) scintillator relative to Si. The results show that, as the energy increases, σ_F (%) gets higher, and this is expected as the QE of the detector drops at high energy. For example, $\sigma_F = 0.9\%$ for reflection $-3\ 1\ -4$ with $E = 41.7$ keV, in contrast to 2.4% for reflection $-1\ -5\ 0$ with $E = 122.9$ keV.

In order to evaluate the potential of the pnCCD detector in combination with the CsI(Tl) scintillator for X-ray applications by means of energy-dispersive Laue diffraction with ultra-hard X-rays, the moduli of the experimental structure factors $|F_{hkl}^{\text{exp}}|$ were compared with the theoretical values $|F_{hkl}^{\text{theo}}|$ and the results are shown in the last column of Table 1 where $\Delta F = |F_{hkl}^{\text{theo}}| - |F_{hkl}^{\text{exp}}|$ and $|F| = |F_{hkl}^{\text{theo}}|$. The agreement between the experimental and theoretical values is visualized in Fig. 9. The mean relative deviation between the experimental and expected structure-factor magnitudes here is equal to 2.5%, which is much better than those obtained by Send *et al.* (2016, 2009) where a naked pnCCD was used for similar experiments, resulting in mean relative deviations of 11 and 10%, respec-

Table 1

Miller indices, Bragg angles, energies, interplanar distances, and experimental and theoretical moduli of the structure factors of the detected reflections.

The last column indicates the relative deviations between the experimental and theoretical structure-factor moduli.

<i>h k l</i>	2θ	<i>E</i> (keV)	<i>d</i> (Å)	$ F_{hkl}^{exp} $	$ F_{hkl}^{theo} $	$\Delta F/ F $ (%)
−6 4 −6	22.9	63.3	0.49	22.1	21.46	2.98
−7 4 −7	23.6	68.9	0.44	1.9	1.76	7.95
−5 3 −6	18.3	65	0.6	14.5	14.13	2.61
−4 2 −6	11.07	84.4	0.76	31.2	33.86	7.85
−3 −1 −4	14.1	46.6	1.08	27.9	28.15	0.88
−1 5 0	13.6	73.4	0.71	24.6	25.68	4.20
−2 3 −3	8.6	83.8	0.98	24.1	23.93	0.71
−3 0 −5	6.3	102.6	1.1	22.9	23.6	2.96
−4 −2 −6	8.7	107	0.76	31.6	33.86	6.67
−3 −3 −4	9.5	90.6	0.82	21.8	22.24	1.97
−1 −5 0	8.13	122.9	0.71	25.7	25.68	0.07
2 −3 5	6.6	113.8	0.94	19.7	20.61	4.41
2 −4 6	10.8	86.2	0.76	32.4	33.86	4.31
−3 1 −4	15.7	41.7	1.08	28.2	28.15	0.17
2 −1 5	11.8	43.9	1.37	27.5	27.72	0.79
3 −2 7	7.6	106.8	0.88	7.25	7.14	1.54
5 −1 12	11.1	108.7	0.59	1.1	1.05	4.76
5 3 12	11.7	112.7	0.53	0.9	0.9	0
4 4 10	12.5	99.2	0.57	3.8	3.78	0.52
4 3 9	8.5	129.1	0.64	2.6	2.62	0.76
4 3 11	17.8	64.6	0.62	21.6	21.78	0.82
4 −1 11	18.2	55.9	0.68	25.9	25.82	0.30
4 −3 11	15.1	77.1	0.6	21.7	21.78	0.36
4 1 11	19.3	52.7	0.7	25.1	25.82	2.78
6 −5 17	16.1	112.7	0.39	10.3	10.44	1.34
6 5 17	19	95.4	0.4	11.1	10.44	6.32
−6 −4 −6	19.8	73.1	0.48	21.5	21.46	0.18
−4 1 −5	18.2	47.1	0.84	17.9	18.29	2.13
4 5 11	14.7	89.9	0.51	15.9	16.75	5.07
−4 −1 −5	17	50.4	0.83	18.5	18.29	1.14
6 −1 15	13.5	108.7	0.48	8.4	8.22	2.18

tively, and is in good agreement with the results obtained by Shokr *et al.* (2017) where a pnCCD + CsI(Tl) system was used. Again, this improvement in accuracy is mainly due to the high QE provided by the CsI(Tl) scintillator in the detector system in a high energy range (50% at 100 keV).

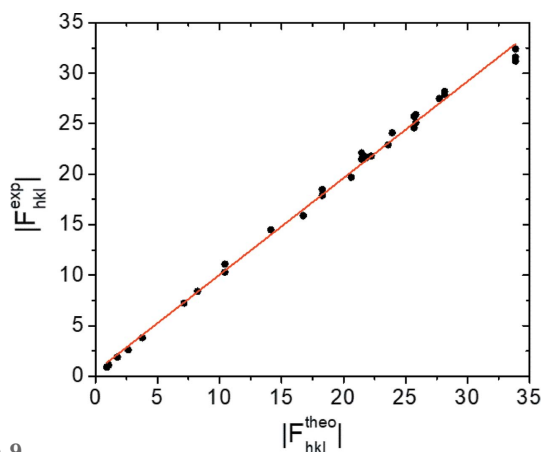


Figure 9 Experimental structure-factor moduli versus theoretical values. The experimental values were obtained from the intensities of the indirect peaks

4. Conclusion

In this paper we have determined the lattice parameters and unit-cell orientation of SrLaAlO₄ using an ultra-high-energy white X-ray beam ranging between 40 and 130 keV and a pnCCD detector coupled to a CsI(Tl) scintillator. The calculations were performed without any prior information. After a scan of an area of 5 cm × 3 cm around the beam centre, about 130 Laue spots were detected. Reflections produced by photons with an energy higher than 90 keV were detected indirectly, while those with lower energy could be detected directly and indirectly at the same time.

Using the advantages of detecting spots at high energies with high intensity and high position resolution, the lattice parameters of the tetragonal unit cell could be determined with an accuracy of better than 0.7% for the basis vectors and less than 0.4% for the enclosed angles. Subsequently, the Laue pattern could be indexed and the moduli of the structure factors were determined from the integrated intensities of the indirect peaks with an error of between 0.9% and 2.4% and a mean deviation of 2.5% relative to the theoretical values.

The results achieved in this work constitute a promising base for further crystallographic applications at ultra-high X-ray energies using a pnCCD detector coupled to a columnar structure CsI(Tl) scintillator.

Funding information

Funding for this research was provided by: Bundesministerium für Bildung und Forschung.

References

Abboud, A., Send, S., Pashniak, N., Leitenberger, W., Ihle, S., Huth, M., Hartmann, R., Strüder, L. & Pietsch, U. (2013). *J. Instrum.* **8**, P05005.

Alghabi, F., Send, S., Schipper, U., Abboud, A., Pashniak, N., Pietsch, U. & Kolb, A. (2014). *J. Instrum.* **9**, T11003.

Brown, P. J., Fox, A. G., Maslen, E. N., O’Keefe, M. A. & Willis, B. T. M. (2004). *International Tables for Crystallography*, Vol. C, *Intensity of Diffracted Intensities*, pp. 554–595. Dordrecht: Springer Netherlands.

Cornaby, S., Szebenyi, D. M. E., Smilgies, D.-M., Schuller, D. J., Gillilan, R., Hao, Q. & Bilderback, D. H. (2010). *Acta Cryst.* **D66**, 2–11.

Dejoie, C., McCusker, L. B., Baerlocher, C., Kunz, M. & Tamura, N. (2013). *J. Appl. Cryst.* **46**, 1805–1816.

Delaunay, B. (1933). *Z. Kristallogr.* **84**, 109–149.

Devanathan, R., Corrales, L., Gao, F. & Weber, W. (2006). *Nucl. Instrum. Methods Phys. Res. A*, **565**, 637–649.

Gauss, C. F., Waterhouse, W., Clarke, A. A., Brinkhuis, J. & Greiter, C. (1986). *Disquisitiones Arithmeticae*. New York: Springer.

Genzel, C., Denks, I., Gimmeier, J., Klaus, M. & Wagener, G. (2007). *Nucl. Instrum. Methods Phys. Res. A*, **578**, 23–33.

Granato, S., Andritschke, R., Elbs, J., Meidinger, N., Struder, L., Weidenspointner, G., Krumrey, M. & Scholze, F. (2013). *IEEE Trans. Nucl. Sci.* **60**, 3150–3157.

Helliwell, J. R. (1984). *Rep. Prog. Phys.* **47**, 1403–1497.

Hofmann, F., Song, X., Abbey, B., Jun, T. S. & Korsunsky, A. M. (2012). *J. Synchrotron Rad.* **19**, 307–318.

Jakoncić, J., Di Michiel, M., Zhong, Z., Honkimaki, V., Jouanneau, Y. & Stojanoff, V. (2006). *J. Appl. Cryst.* **39**, 831–841.

Jing, Z., Huda, W., Walker, J. K. & Choi, W. Y. (1998). *Proc. SPIE*, **3336**, doi:10.1117/12.317062.

- Kirkwood, H. J., de Jonge, M. D., Howard, D. L., Ryan, C. G., van Riessen, G., Hofmann, F., Rowles, M. R., Paradowska, A. M. & Abbey, B. (2017). *Powder Diffr.* **32**(4)(Suppl.), S16.
- Kraft, P., Bergamaschi, A., Broennimann, Ch., Dinapoli, R., Eikenberry, E. F., Henrich, B., Johnson, I., Mozzanica, A., Schlepütz, C. M., Willmott, P. R. & Schmitt, B. (2009). *J. Synchrotron Rad.* **16**, 368–375.
- Lange, J. (1995). *Acta Cryst.* **A51**, 559–565.
- Leitenberger, W., Hartmann, R., Pietsch, U., Andritschke, R., Starke, I. & Strüder, L. (2008). *J. Synchrotron Rad.* **15**, 449–457.
- Lindholm, E., Nickolls, J., Oberman, S. & Montrym, J. (2008). *IEEE Micro*, **28**, 39–55.
- Liss, K.-D., Bartels, A., Schreyer, A. & Clemens, H. (2003). *Textures Microstruct.* **35**, 219–252.
- Medjoubi, K., Thompson, A., Béar, J.-F., Clemens, J.-C., Delpierre, P., Da Silva, P., Dinkespiler, B., Fourme, R., Gourhant, P., Guimaraes, B., Hustache, S., Idir, M., Itié, J.-P., Legrand, P., Meneglier, C., Mercere, P., Picca, F. & Samama, J.-P. (2012). *J. Synchrotron Rad.* **19**, 323–331.
- Minkowski, H. (1891). *J. Reine angew. Math. (Crelles J.)*, **107**, 278–297.
- Nagarkar, V. V., Gupta, T. K., Miller, S. R., Klugerman, Y., Squillante, M. R. & Entine, G. (1998). *IEEE Trans. Nucl. Sci.* **45**, 492–496.
- Schlosser, D., Hartmann, R., Kalok, D., Bechteler, A., Abboud, A., Shokr, M., Çonka, T., Pietsch, U. & Strüder, L. (2017). *J. Instrum.* **12**, P04009.
- Schlosser, D., Huth, M., Hartmann, R., Abboud, A., Send, S., Çonka-Nurdan, T., Shokr, M., Pietsch, U. & Strüder, L. (2016). *Nucl. Instrum. Methods Phys. Res. A*, **805**, 55–62.
- Send, S. (2013). *Utilization of a Frame-store pnCCD for Energy-dispersive Laue Diffraction with White Synchrotron Radiation*. PhD thesis, University of Siegen, Germany.
- Send, S., Abboud, A., Hartmann, R., Huth, M., Leitenberger, W., Pashniak, N., Schmidt, J., Strüder, L. & Pietsch, U. (2013). *Nucl. Instrum. Methods Phys. Res. A*, **711**, 132–142.
- Send, S., Abboud, A., Leitenberger, W., Weiss, M. S., Hartmann, R., Strüder, L. & Pietsch, U. (2012). *J. Appl. Cryst.* **45**, 517–522.
- Send, S., Abboud, A., Wiesner, N., Shokr, M., Klaus, M., Genzel, C., Conka-Nurdan, T., Schlosser, D., Huth, M., Hartmann, R., Strüder, L. & Pietsch, U. (2016). *J. Appl. Cryst.* **49**, 222–233.
- Send, S., von Kozierowski, M., Panzner, T., Gorfman, S., Nurdan, K., Walenta, A. H., Pietsch, U., Leitenberger, W., Hartmann, R. & Strüder, L. (2009). *J. Appl. Cryst.* **42**, 1139–1146.
- Shokr, M., Schlosser, D., Abboud, A., Algashi, A., Tosson, A., Çonka, T., Hartmann, R., Klaus, M., Genzel, C., Strüder, L. & Pietsch, U. (2017). *J. Instrum.* **12**, P12032.
- Tosson, A., Shokr, M., Abboud, A., Bebawy, Y., Algashi, A., Hartmann, R., Klaus, M., Genzel, C., Strüder, L. & Pietsch, U. (2019). *J. Instrum.* **14**, P01008.
- Villars, P. & Cenzual, K. (2012). Editors. *SrLaAlO₄ Crystal Structure*. Datasheet from Pauling File Multinaries ed. 2012, data set ID sd_0544036. In SpringerMaterials, https://materials.springer.com/isp/crystallographic/docs/sd_0544036. Copyright 2016 Springer-Verlag Berlin/Heidelberg, Germany, and Material Phases Data System (MPDS), Switzerland, and National Institute for Materials Science (NIMS), Japan.
- Wilson, A. J. C. (1949). *Acta Cryst.* **2**, 318–321.
- Wu, Y.-H., Chang, Y.-Y., Tsai, Y.-W. & Chang, S.-L. (2016). *J. Appl. Cryst.* **49**, 1653–1658.